Thin film growth of the Weyl semimetal NbAs

Wilson Yáñez-Parreño [1], Yu-Sheng Huang,[1] Supriya Ghosh,[2] Saurav Islam [1], Javier E. Gómez,[3,4] Emma Steinebronn,[1]
Anthony Richardella,[1,5] Luis Avilés-Félix,[3,4,6] Alejandro Butera,[3,4,6] K. Andre Mkhoyan,[2] and Nitin Samarth[1,5,*]

[1]*Department of Physics, Pennsylvania State University, University Park, Pennsylvania 16802, USA*

[2]*Department of Chemical Engineering and Materials Science, University of Minnesota, Minneapolis, Minnesota 55455, USA*

[3]*Instituto de Nanociencia y Nanotecnología (CNEA - CONICET), Nodo Bariloche, Av. Bustillo 9500,*
(8400) S. C. de Bariloche (RN), Argentina

[4]*Lab. Resonancias Magnéticas, Gerencia de Física, Centro Atómico Bariloche, Av. Bustillo 9500, (8400) S. C. de Bariloche (RN), Argentina*

[5]*Materials Research Institute, Pennsylvania State University, University Park, Pennsylvania 16802, USA*

[6]*Instituto Balseiro, CNEA-UNCuyo, Av. Bustillo 9500, (8400) S. C. de Bariloche (RN), Argentina.*

We report the synthesis and characterization of thin films of the Weyl semimetal NbAs grown on GaAs (100) and As-terminated GaAs (111)B substrates. By choosing the appropriate substrate, we can stabilize the growth of NbAs in the [001] and [100] directions. We combine x-ray characterization with high-angle annular dark field scanning transmission electron microscopy to understand both the macroscopic and microscopic structure of the NbAs thin films. We show that these films are textured with domains that are tens of nanometers in size and that, on a macroscopic scale, are mostly aligned to a single crystalline direction. We describe electrical transport measurements that reveal similar behavior in films grown in both crystalline orientations, namely resistivity in the range 420–450 $\mu\Omega$ cm and carrier densities in the range $\sim 10^{21}$–10^{22} cm^{-3} at 2 K. Finally we measure spin to charge conversion in NbAs and show that it qualitatively agrees with first principles calculations.

I. INTRODUCTION

The TX class (T=Ta/Nb X=As/P) of transition metal monopnictides is a promising quantum materials platform for studying topological phenomena of contemporary interest because the bulk band structure corresponds to that of a topological Weyl semimetal [1–4]. Broken inversion symmetry in this class of materials leads to Weyl nodes with different chiralities; when projected onto the surface of the crystal, these nodes are connected by topological surface states (Fermi arcs) [1,2,4–6]. Interesting physical phenomena observed in these canonical Weyl semimetals include the chiral anomaly in charge transport, transport in the quantum limit under high magnetic fields, phase transitions between different topological states, strong intrinsic spin Hall effect, and symmetry-induced nontrivial spin-orbit torque [5,7–10]. Prior studies of this family of topological semimetals have primarily focused on bulk single crystal samples; while these are of high structural quality, thin film samples grown on substrates compatible with standard semiconductor processing are more desirable if these Weyl semimetals are to become useful for technological applications [3,11]. This is especially true in topological materials where certain macroscopic properties like spin-momentum correlation are topologically protected and enforced by symmetry in a way that is robust against disorder [12–15]. An extreme example is the recent recognition that topological aspects of the electronic states persist even in amorphous Bi$_2$Se$_3$ [13]. In the specific case

of spintronics applications, it is acceptable to compromise on the single crystalline quality due to short spin diffusion lengths (a few nm). For example, manufacturing processes in the spintronics industry routinely use sputtered polycrystalline thin films for information storage applications such as spin valves for read heads and spin transfer torque magnetic random access memory. In the context of topological spintronics, efficient charge-spin interconversion has been demonstrated in polycrystalline textured films of topological insulators[16], Weyl semimetals [17], and Dirac semimetals [18]. Thin films are also desirable because of the possibility of modulating the band structure, studying proximity induced phenomena, or controlling the crystalline orientation by substrate strain [19–21]. The last is particularly important because transition metal monopnictides are expected to have anisotropic observables that follow their tetragonal crystal symmetry due to Neumann's principle [22,23]. It is thus of fundamental interest to have large area thin film Weyl semimetal samples with a well defined and controlled macroscopic crystalline orientation if such physics is to be explored.

In this context, the synthesis of thin films of TaAs, TaP, and NbP has been achieved recently using molecular beam epitaxy (MBE) and pulsed laser deposition with different structural qualities [15,24–26]. In this study, we develop the synthesis of NbAs thin films on a GaAs substrate using MBE. We show that the growth of NbAs along different crystalline directions can be stabilized by judicious choice of the substrate direction. We then use x-ray diffraction to understand the macroscopic structure of the films, in addition to characterization using atomic force microscopy and electrical transport measurements. We use high-angle annular dark-field

* nsamarth@psu.edu
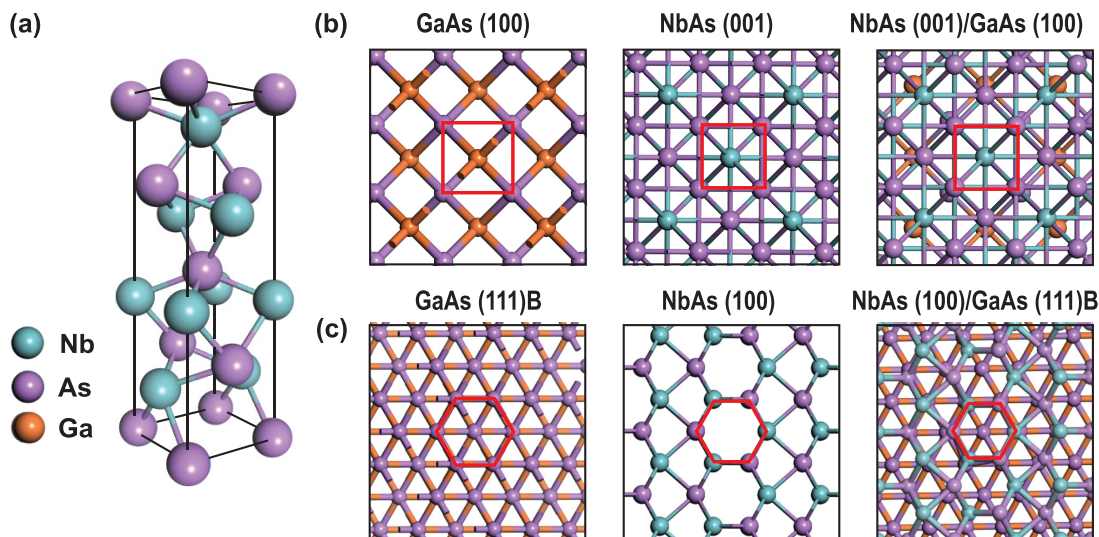
FIG. 1. (a) Crystal structure of NbAs. (b) Top view of GaAs (100), NbAs (001), and NbAs (001) on top of GaAs (100). (c) Top view of GaAs (111)B, NbAs (100), and NbAs (100) on top of GaAs (111)B. We show the square and hexagonal symmetry and lattice mismatch between the films and the substrates.

scanning transmission electron microscopy (HAADF-STEM) to show that our films are textured with single crystal domains that are tens of nanometers in size. Finally, we measure spin to charge conversion in NbAs and show that it qualitatively matches the expected results from first principles calculations.

II. RESULTS

A. NbAs thin films grown on III-V substrates

We first discuss the choice of substrate for the growth of NbAs thin films. NbAs is a transition metal monopnictide that has 12 pairs of Weyl nodes in its band structure [1,4,11]. It is a member of the $I4_1md$ space group and crystallizes in a body-centered tetragonal structure [Fig. 1(a)] with a lattice constant of $a = 0.345$ nm and $c = 1.168$ nm [1,2,11]. It is difficult to find an appropriate lattice-matched substrate with a lattice constant in this range [27]. Based on previous reports of MBE growth of this family of semimetals [5,15,24,25], we tried using different III-V semiconductors (GaAs, GaP, and InAs) as our substrates. Amongst these, the best results were achieved in GaAs which had a lower lattice mismatch than InAs and, unlike GaP, had the right surface chemistry to promote NbAs growth. In this paper, we focus on studying NbAs films grown on GaAs; further information about characterization of NbAs on other substrates can be found in the Supplemental Material [28].

An analysis of the crystal structure of NbAs suggests that the growth of NbAs (001) can be stabilized by using GaAs (100) as a substrate [Fig. 1(b)]: here, the lattice mismatch is 16% along the $\langle 110 \rangle$ and 18% along the $\langle 100 \rangle$ GaAs directions. Although this is a very large lattice mismatch within the context of epitaxial growth, it is within range to allow NbAs to grow with a 45° rotation with respect to the $\langle 100 \rangle$ GaAs direction. NbAs (100) has a similar relationship with GaAs (111) as a substrate: Fig. 1(c) shows that if we superimpose both lattices, the NbAs atoms roughly align with the hexagonal structure of GaAs (111) with a 17% mismatch on each side.

We carry out the synthesis of the NbAs films in a VEECO 930 MBE chamber while monitoring the growth using reflection high energy electron diffraction (RHEED) at 12 keV (Fig. 2). We desorb the native oxide on an epiready semiinsulating GaAs substrate and then grow 30 nm of GaAs at a thermocouple temperature of 720 °C. This corresponds to 540 °C measured using the temperature dependent optical absorption edge of GaAs. We used Ga (5N) and As (5N)
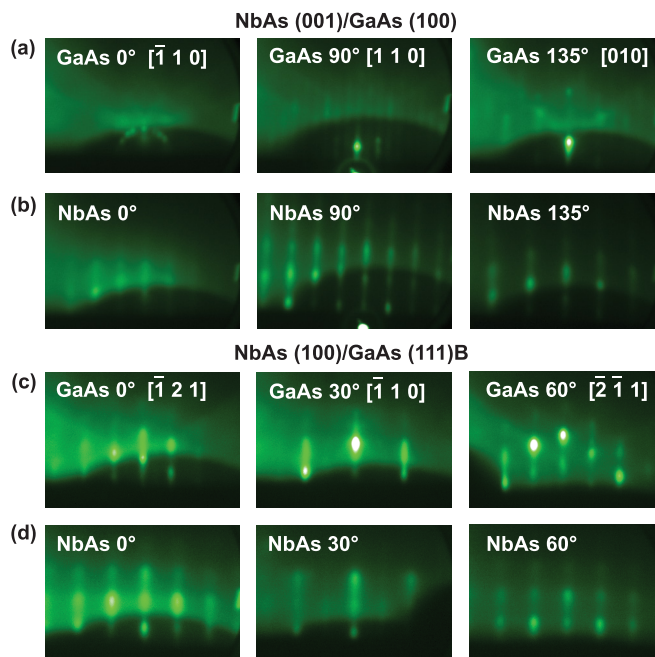
FIG. 2. RHEED pattern of (a) GaAs (100) substrate along the [$\bar{1}$10], [110], and [010] directions. (b) NbAs (001) thin film along the same directions as (a), (c) GaAs (111)B substrate along the [$\bar{1}$21], [$\bar{1}$10], and [$\bar{2}\bar{1}$1] directions, and (d) NbAs (100) thin film along the same directions as (c).
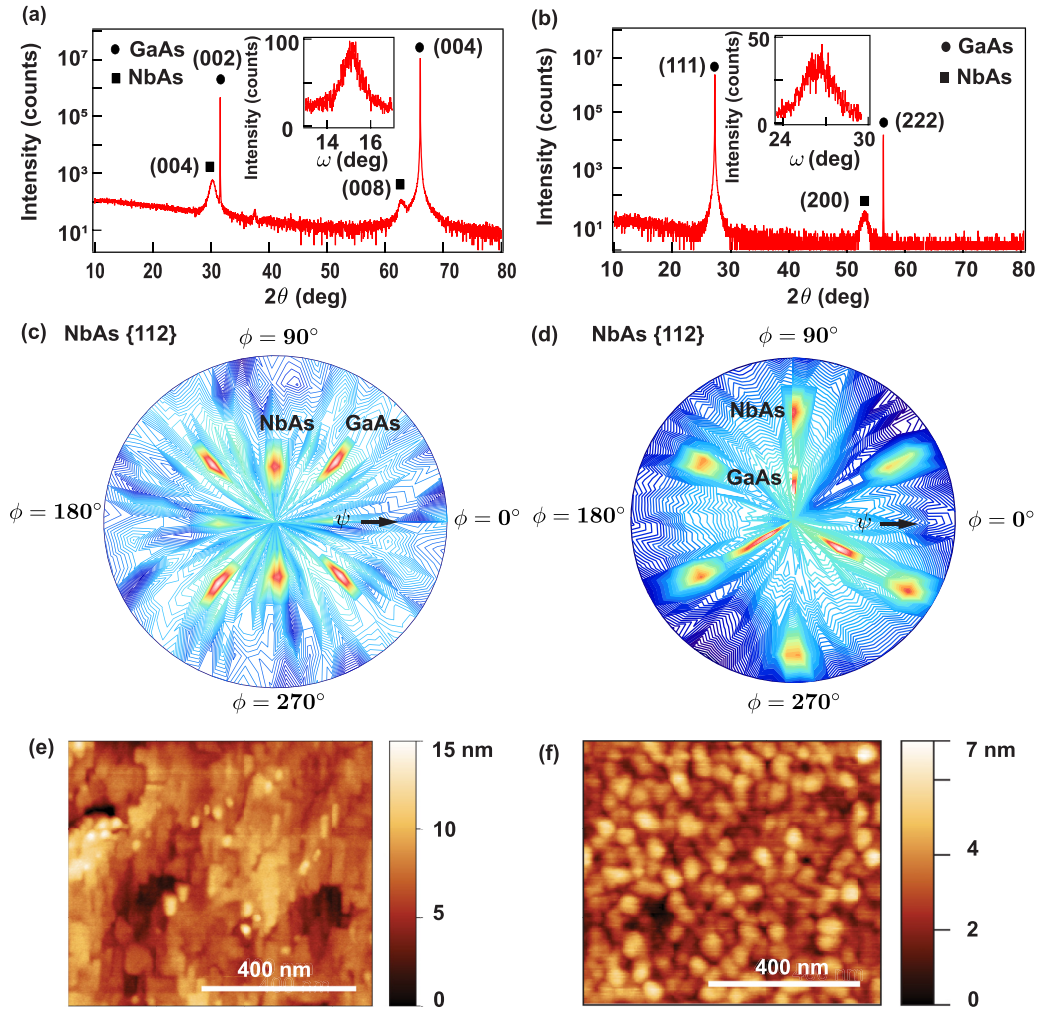
FIG. 3. X-ray diffraction $2\theta - \omega$ scan of NbAs grown on (a) GaAs (100) and (b) GaAs (111)B. Pole figures around the NbAs {112} direction for samples grown on (c) GaAs (100) and (d) GaAs (111)B. Atomic force microscopy image of (e) NbAs (001) and (f) NbAs (100) showing a root mean square (RMS) surface roughness of 1.4 nm and 0.9 nm, respectively.

sources evaporated from standard effusion cells. The As:Ga beam equivalent pressure ratio is ~14 (as measured using an ion gauge). After this, we cool down the substrate to a thermocouple temperature of 400 °C in the presence of As flux. At this point, we observed a RHEED pattern showing a 2×4 surface reconstruction for GaAs (100) [Fig. 2(a)] and a C6 symmetry for As terminated GaAs (111)B [(Fig. 2(c)]. We chose As-terminated GaAs (111)B substrates instead of Ga-terminated GaAs (111)A because this requires a lower As flux during GaAs desorption and growth. This allows us to obtain an optimal growth rate while also minimizing As vacancies during growth. We then increase the substrate temperature to 700–750 °C (measured by a thermocouple in the substrate manipulator) and simultaneously deposit As and Nb (the latter from a SPECS EBE-4 4 pocket e-beam evaporator), obtaining the RHEED pattern shown in Figs. 2(b) and 2(d). In the case of NbAs grown on GaAs (100) [Fig. 2(b)], the RHEED pattern is different in the [110] and [1$\bar{1}$0] directions. This follows the C_2 symmetry of the GaAs substrate in the 2×4 reconstruction. In the case of NbAs grown on GaAs (111)B [Figs. 2(c) and 2(d)], the NbAs RHEED pattern is the same in the GaAs [1$\bar{2}$1] and [2$\bar{1}\bar{1}$] crystal directions which

are 60° apart. This indicates a C_6 symmetry in the NbAs thin film due to twinning during growth.

B. Macroscopic structural characterization of the NbAs thin films

To characterize our films on a macroscopic scale, we use x-ray diffraction. First, we perform a coupled $2\theta - \omega$ scan on NbAs grown on GaAs (100) [Fig. 3(a)] and detect the presence of diffraction peaks from NbAs (001). Second, we perform a similar scan on NbAs grown on GaAs (111)B [Fig. 3(b)] and detect the presence of NbAs (100). We notice that there is a small peak at 37.5° in NbAs (001) corresponding to strained cubic Nb (110). This is suppressed in NbAs (100). We emphasize that these different crystalline planes are not equivalent due to the tetragonal crystal structure of NbAs (Fig. 1). To quantify the degree of crystallinity in our films, we perform a rocking curve (ω scan) around the NbAs peaks and obtain a full width half maximum (FWHM) of 1.3° for NbAs (001) and 2.1° for NbAs (100). To understand the planar structure of our films, we measure a pole figure around the NbAs {112} direction. We observe the presence of two
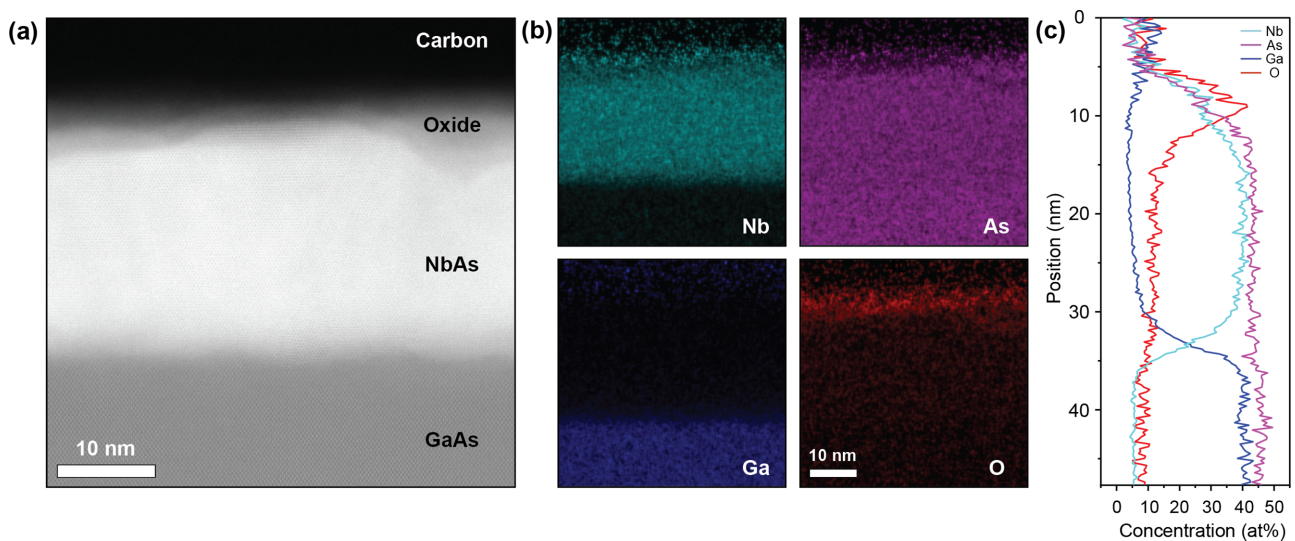
FIG. 4. (a) HAADF-STEM image of the NbAs (001) thin film on a GaAs substrate. (b) STEM-EDX elemental maps of Nb, As, Ga, and O in the film. (c) Concentration of the elements in (a) across the NbAs/GaAs interface.

different sets of peaks corresponding to the GaAs reflection of copper $K\beta$ and NbAs $K\alpha$ radiation. We find that NbAs (001) stabilizes with a 45° rotational offset with respect to the basal plane [Fig. 3(c)]. As stated before, this is due to the lower lattice mismatch in the GaAs $\langle 110 \rangle$ direction. This agrees with previous reports of TaP and NbP grown on a substrate with cubic crystal structure and high lattice mismatch [25]. The difference in intensity between the peaks at 0° and 90° suggests that there is a preferred direction of alignment of the domains in the sample, probably due to the 2×4 GaAs surface reconstruction achieved before the growth. In Fig. 3(d), we see the presence of three dominant GaAs peaks with the expected C_3 symmetry of GaAs in the (111) direction. We also see the presence of six NbAs peaks that are 60° apart. This indicates the presence of domains (twins) that are rotated by 60° with respect to each other. Finally, to understand the structure of the surface of the films, we use atomic force microscopy (AFM) imaging on these samples. In both surfaces [Figs. 3(e) and 3(f)] we see domains that are tens of nanometers in size. The main difference between these different surfaces is that in the (001) plane we see the presence of a rougher surface with domains that show the tetragonal structure of NbAs, while in the (100) direction, we have a smoother surface with a higher degree of disorder. This qualitatively agrees with the larger FWHM obtained in the rocking curve in NbAs (100).

C. Microscopic structural characterization of the NbAs thin films

To understand the microscopic structure of NbAs in the thin film regime, we use HAADF-STEM imaging and energy-dispersive x-ray spectroscopy (STEM-EDX). The results shown in the present manuscript correspond to NbAs (001) grown on GaAs (100). Similar measurements are obtained for NbAs (100)/GaAs (111)B. Figure 4(a) shows a cross-section HAADF-STEM image of NbAs on GaAs. The NbAs layer is polycrystalline with grain sizes in the range of tens of

nanometers, in agreement with the XRD results. The interface between the NbAs and GaAs is diffuse and shows interdiffusion, likely due to the high temperatures required to grow NbAs and the large lattice mismatch with GaAs. The relative concentration of Nb:As and Ga:As is 1:1 in both layers, which confirms the absence of other phases [Figs. 4(b) and 4(c)]. We note that the surface of the films quickly oxidizes under ambient atmosphere. HAADF-STEM shows a self-limited oxide layer that covers the top $\sim$3 nm of the NbAs film. This is consistent with our previous studies of other topological semimetals such as TaAs and Cd_3As_2 [5,17]. This oxidation process is a serious limitation for characterization techniques and applications that rely on interacting with the surface of the films. It also indicates caution when attributing the origins of unusual physical phenomena to surface states since they could easily be the result of the states associated with this oxidation layer [5]. To study the intrinsic physical phenomena of Weyl semimetals, oxidation should be avoided at all costs by either careful capping or ultrahigh vacuum transfer of the films.

The polycrystalline NbAs layer has domains oriented along the major crystal directions, in addition to the presence of some grain boundaries and twins [Fig. 5(a)]. Two such examples are shown in Fig. 5(b) which are commonly observed in the thin films grown on GaAs. Comparison of the fast Fourier transforms (FFTs) from the grains to the simulated FFTs confirms the two grains to be along the [001] and [100] directions, respectively [Figs. 5(c) and 5(d)]. We note that this is a small subset of several different domains that were identified in NbAs that had more complex orientations that were harder to identify. We believe that more complex microscopy techniques that go beyond the scope of this work (i.e., in-plane imaging or statistical analysis of domain orientation) are needed to fully understand the structure of the domains in NbAs thin films.

D. Electrical transport in NbAs thin films

We also characterized the electrical transport properties of the NbAs thin films by fabricating Hall bars using standard
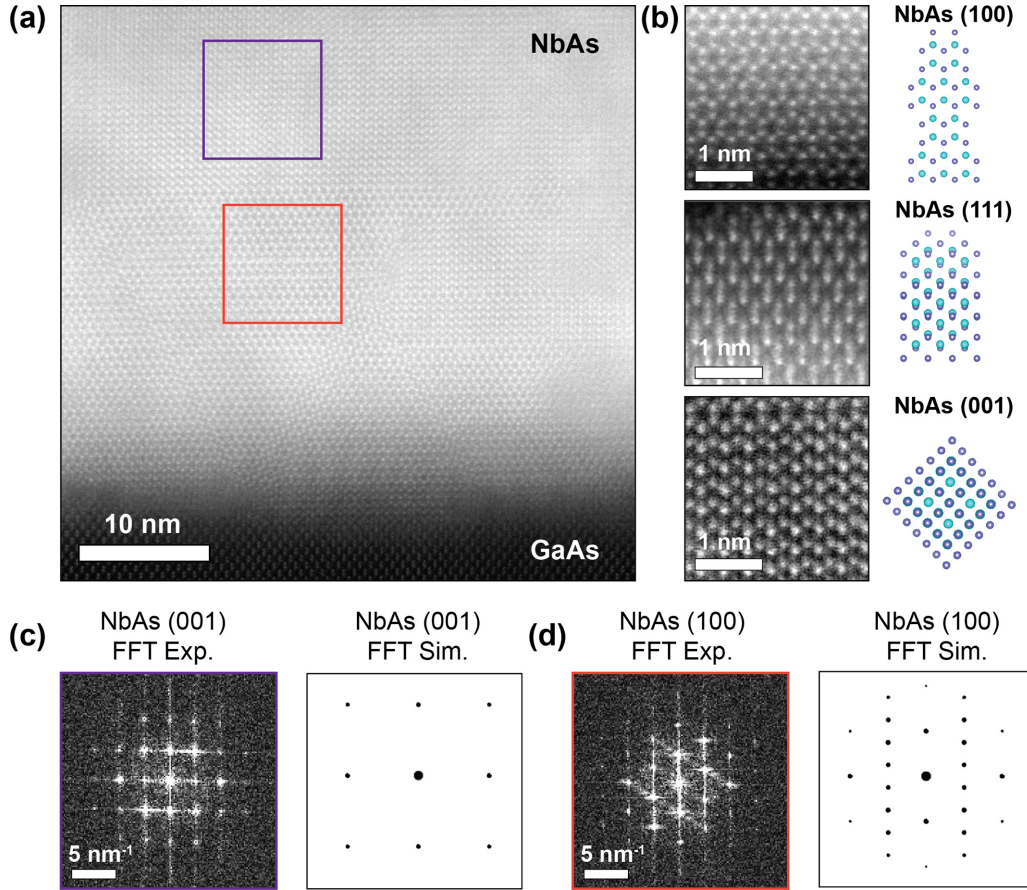
FIG. 5. (a) HAADF-STEM image of NbAs showing polycrystalline structure with multiple grains along different crystal orientations. (b) Common NbAs orientations observed in grains along with the structural model. (c) and (d) FFT of the NbAs grains highlighted by the purple and orange boxes respectively along with the simulated FFTs for the (001) and (100) orientations.

photolithography and Ar plasma etching. The dimensions of the Hall bar devices (length, width, and thickness) are 1000 μm × 500 μm × 23 nm for NbAs (001) and 40 μm × 10 μm × 10 nm for NbAs (100). Even though these devices have different dimensions and were measured with different current densities, it can be seen that both of them show similar qualitative and quantitative behavior. The resistivity (ρ) vs temperature (T) in both samples shows activated behavior [Figs. 6(a) and 6(b)], possibly arising from defects. Hall measurements performed at $T = 2$ K show linear dependence with the magnetic field (B) within the range investigated (± 5 T), and electrons to be the dominant carrier in both samples [Figs. 6(c) and 6(d)], with a carrier density (n) 6.5 × 10^{22} cm^{-3} for NbAs (001) and 5 × 10^{21} cm^{-3} in NbAs (100). This is different from TaAs thin films grown in a similar manner where holes are the primary carrier (see the Supplemental Material)[28] [5]. This suggests that it might be possible to control the position of the Fermi level in NbAs by introducing Ta doping. The mobility was calculated using $\mu = \frac{\sigma}{ne}$, where σ is the conductivity at $B = 0$ T and e is the electronic charge, with $\mu = 0.2$ and 3 cm^2 (V · s)$^{-1}$ for NbAs (001) and NbAs (100), respectively. The differences in mobility and carrier density is probably due to the differences in thickness between samples. Such strong dependence has also been shown in TaAs thin films with similar quality, which show reduced mobilities in the ultrathin regime [15]. The Fermi

wavelength (k_f) calculated using $k_f = (3\pi^2 n)^{\frac{1}{3}}$ is $\approx 5 \times 10^9$ m^{-1} while the mean free path (l_m), calculated using $l_m = \mu \hbar k_f / e$ varies between $10^{-9} - 10^{-10}$ m. With these values we find that $k_f l_m = 2.7$ and 6.8 for the samples, respectively. We also performed longitudinal magnetoresistance measurements at $T = 2$ K, which showed positive magnetoresistance in both samples [Figs. 6(c) and 6(d)]. Since $k_f l_m$ satisfies the limit for diffusive transport conditions, as set by the Ioffe-Regel limit ($k_f l_m \approx 1$), we estimated the phase breaking length (l_ϕ) in both films by extracting the quantum correction to conductivity and fitting it with the Hikami-Larkin-Nagaoka expression [29,30] for weak antilocalization for high spin-orbit coupled systems:

$$\triangle \sigma = \alpha \frac{e^2}{\pi h} \left[\psi \left(\frac{1}{2} + \frac{B_\phi}{B} \right) - \ln \left(\frac{B_\phi}{B} \right) \right]. \quad (1)$$

Here, B_ϕ is the phase coherence field, and α is a fitting parameter. We estimate $l_\phi = \sqrt{\frac{\hbar}{4eB_\phi}}$ to be 50–80 nm in both films. Further investigation of electrical properties will be carried out in the future in a broader range of samples to explore the electrical properties of these materials.

E. Spin to charge conversion in NbAs

As a first step to study the possible technological applications of NbAs, we carried out spin pumping measurements
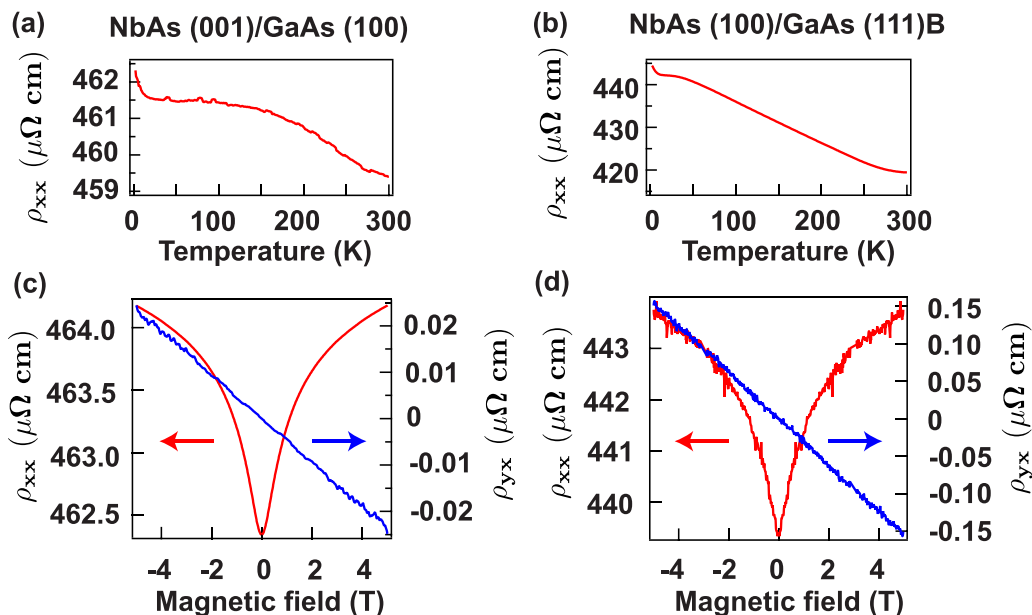
FIG. 6. (a) and (b) Longitudinal resistivity (ρ_{xx}) as a function of temperature in 23 nm thick NbAs (001) and 10 nm thick NbAs (100). (c) and (d) Longitudinal resistivity (ρ_{xx}) and Hall resistivity (ρ_{yx}) as a function of magnetic field in NbAs (001) and (100).

in a NbAs (001)/permalloy (Py) heterostructure. For this, the NbAs films were transferred under ultrahigh vacuum to a second chamber for the deposition of the ferromagnet using a vacuum suitcase. This suppresses the possible formation of oxide at the interface that might affect the spin transport across the NbAs/Py interface [5,17]. We placed the heterostructure in a microwave cavity (X-band 9.6 GHz) and applied a radiofrequency signal while sweeping an in plane external magnetic field [Fig. 7(a)]. The external magnetic field excites the ferromagnet, generating precession of its magnetization. This can be measured as a change in the absorbed power under resonance conditions [Fig. 7(c)]. Simultaneously, we probe the voltage in the edges of the sample [Figs. 7(b) and 7(c)] and measure a large signal when the magnetization is precessing [17,31,32]. We observe that this signal increases linearly with power [Fig. 7(d)] and switches sign under magnetic field reversal. This is consistent with spin to charge conversion due to spin pumping from the ferromagnet into the topological semimetal. The measured voltage follows the symmetry predicted by the inverse spin Hall effect (ISHE) and the inverse Rashba-Edelstein effect (IREE), i.e., $\vec{E} \propto \vec{J}_S \times \vec{\sigma}$, where $\vec{E}$ is the electric field produced in the sample, $\vec{J}_s$ is the spin current flowing from the ferromagnet into the topological semimetal, and $\vec{\sigma}$ is the direction of spin polarization [17,31,32]. Taking both of these phenomena into consideration, we find that the charge current (J_C) generated in the heterostructure is

$$J_C = \frac{Vsp}{\text{w}R} = \left[\theta_{SH} \lambda_{SD} \tanh \left(\frac{t_{\text{NbAs}}}{2\lambda_{SD}} \right) + \lambda_{\text{IREE}} \right] J_S, \quad (2)$$

where Vsp is the measured voltage due to spin pumping, w is the width of the sample, R its resistance, θ_{SH} is the spin Hall angle, λ_{SD} is the spin diffusion length, t_{NbAs} is the thickness of the topological semimetal, and λ_{IREE} is the inverse Rashba-Edelstein effective length [17,31,32].

Precisely determining each of these parameters, characterizing the magnetic properties of the ferromagnet, and

calculating the contribution of the inverse spin Hall effect and the inverse Rashba-Edelstein effect to the measured phenomena requires more systematic measurements that go beyond the present study. Nevertheless, we clearly show spin to charge conversion in the topological semimetal NbAs, making it a promising candidate for spintronic applications. We suspect that optimization of Py growth conditions is likely to lead to even higher spin-to-charge current conversion which is highly desired for technology. If we assume that the predominant contribution to the measured signal is due to the spin Hall effect, we obtain a positive spin Hall angle, and a positive spin Hall conductivity in electron-type NbAs, that is opposite to hole-type TaAs control samples (see the Supplemental Material). This agrees with first principles calculations of both NbAs and TaAs that show a positive spin Hall conductivity when the Fermi level is in the conduction band that changes sign when the Fermi level is in the valence band [10]. This implies that the spin to charge conversion efficiency in NbAs can be tuned by changing the position of the Fermi level when introducing Ta into NbAs. It is also possible to study how crystalline orientation affects the spin to charge conversion phenomena by performing similar experiments in NbAs (100).

III. CONCLUSION

In summary, we report the synthesis by MBE of Weyl semimetal NbAs thin films on GaAs substrates, a semiconductor of relevance for optoelectronics. We show that different NbAs crystalline orientations can be stabilized by choosing the appropriate substrate orientation. The large lattice mismatch between GaAs and NbAs, coupled with the high growth temperature needed to achieve NbAs growth, induces diffusion at the GaAs/NbAs interface. This hinders the crystallinity of our samples and produces textured films with domains that are tens of nanometers in size. These
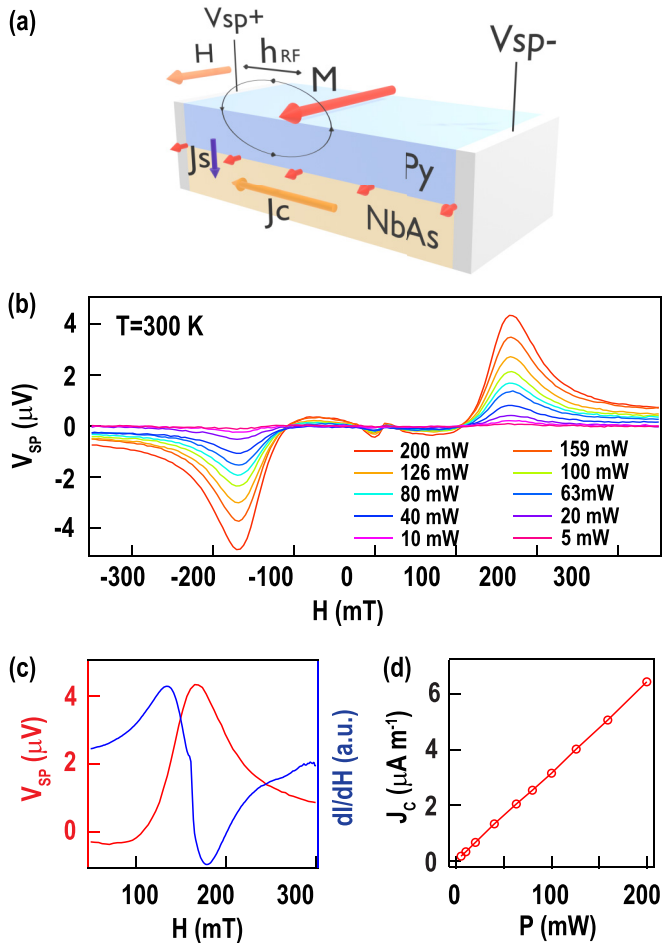
FIG. 7. (a) Illustration of spin to charge conversion due to spin pumping. (b) Voltage signal measured in the NbAs (10 nm)/Py(8 nm) heterostructure at room temperature with different applied microwave power. (c) Spin pumping voltage signal (Vsp) and ferromagnetic resonance absorption spectra (dI/dH) measured at 9.6 GHz and 200 mW. (d) Charge current (J_C) as a function of power showing linear behavior.

to a single crystalline orientation shown in the x-ray diffraction data. We reconcile both measurements by proposing the existence of a preferred crystalline orientation of these domains that can only be seen on a macroscopic scale. More detailed microscopy studies that include statistical analysis and in-plane imaging are required to confirm this hypothesis. We observe that the films naturally oxidize when taken out of vacuum. This effect makes it difficult to access the electronic states of NbAs using surface sensitive techniques like angle resolved photoemission spectroscopy or scanning tunneling spectroscopy that involve the out-of-vacuum transfer of samples between different vacuum chambers. This suggests caution when trying to probe topological surface states in this family of Weyl semimetals in samples with an oxidized surface. We show spin to charge conversion in NbAs (001) at room temperature that qualitatively agrees with first principles calculations. This makes it a promising material to be used in spintronic devices. Finally, we expect that further experimental improvements will allow us to increase the degree of crystallinity in NbAs films so that we are able to explore a broader range of physics in this family of well-established Weyl semimetals.

domains nonetheless have a well defined crystal structure that is oriented in different crystalline directions. Despite the large lattice mismatch, the surface chemistry of GaAs seems to be a decisive factor for effectively nucleating NbAs growth. There is some apparent inconsistency between the textured nature of our films shown in STEM and the clear peaks corresponding

[1] S.-Y. Xu, I. Belopolski, N. Alidoust, M. Neupane, G. Bian, C. Zhang, R. Sankar, G. Chang, Z. Yuan, C.-C. Lee, S.-M. Huang, H. Zheng, J. Ma, D. S. Sanchez, B. Wang, A. Bansil, F. Chou, P. P. Shibayev, H. Lin, S. Jia *et al.*, Discovery of a Weyl fermion semimetal and topological Fermi arcs, Science **349**, 613 (2015).

[2] B. Q. Lv, H. M. Weng, B. B. Fu, X. P. Wang, H. Miao, J. Ma, P. Richard, X. C. Huang, L. X. Zhao, G. F. Chen, Z. Fang, X. Dai, T. Qian, and H. Ding, Experimental discovery of Weyl semimetal TaAs, Phys. Rev. X **5**, 031013 (2015).

[3] S.-Y. Xu, I. Belopolski, D. S. Sanchez, M. Neupane, G. Chang, K. Yaji, Z. Yuan, C. Zhang, K. Kuroda, G. Bian, C. Guo, H. Lu,

T.-R. Chang, N. Alidoust, H. Zheng, C.-C. Lee, S.-M. Huang, C.-H. Hsu, H.-T. Jeng, A. Bansil *et al.*, Spin polarization and texture of the Fermi arcs in the Weyl fermion semimetal TaAs, Phys. Rev. Lett. **116**, 096801 (2016).

[4] S.-M. Huang, S.-Y. Xu, I. Belopolski, C.-C. Lee, G. Chang, B. Wang, N. Alidoust, G. Bian, M. Neupane, C. Zhang, S. Jia, A. Bansil, H. Lin, and M. Z. Hasan, A Weyl fermion semimetal with surface Fermi arcs in the transition metal monopnictide TaAs class, Nat. Commun. **6**, 7373 (2015).

[5] W. Yanez, Y. Ou, R. Xiao, S. Ghosh, J. Dwivedi, E. Steinebronn, A. Richardella, K. A. Mkhoyan, and N. Samarth, Giant

dampinglike-torque efficiency in naturally oxidized polycrystalline TaAs thin films, Phys. Rev. Appl. **18**, 054004 (2022).

[6] X. Yuan, Z. Yan, C. Song, M. Zhang, Z. Li, C. Zhang, Y. Liu, W. Wang, M. Zhao, Z. Lin, T. Xie, J. Ludwig, Y. Jiang, X. Zhang, C. Shang, Z. Ye, J. Wang, F. Chen, Z. Xia, D. Smirnov *et al.*, Chiral landau levels in Weyl semimetal NbAs with multiple topological carriers, Nat. Commun. **9**, 1854 (2018).

[7] X. Yuan, C. Zhang, Y. Zhang, Z. Yan, T. Lyu, M. Zhang, Z. Li, C. Song, M. Zhao, P. Leng, M. Ozerov, X. Chen, N. Wang, Y. Shi, H. Yan, and F. Xiu, The discovery of dynamic chiral anomaly in a Weyl semimetal NbAs, Nat. Commun. **11**, 1259 (2020).

[8] D. A. Kealhofer, L. Galletti, T. Schumann, A. Suslov, and S. Stemmer, Topological insulator state and collapse of the quantum Hall effect in a three-dimensional Dirac semimetal heterojunction, Phys. Rev. X **10**, 011050 (2020).

[9] B. J. Ramshaw, K. A. Modic, A. Shekhter, Y. Zhang, E.-A. Kim, P. J. W. Moll, M. D. Bachmann, M. K. Chan, J. B. Betts, F. Balakirev, A. Migliori, N. J. Ghimire, E. D. Bauer, F. Ronning, and R. D. McDonald, Quantum limit transport and destruction of the Weyl nodes in TaAs, Nat. Commun. **9**, 2217 (2018).

[10] Y. Sun, Y. Zhang, C. Felser, and B. Yan, Strong intrinsic spin Hall effect in the TaAs family of Weyl semimetals, Phys. Rev. Lett. **117**, 146403 (2016).

[11] S.-Y. Xu, N. Alidoust, I. Belopolski, Z. Yuan, G. Bian, T.-R. Chang, H. Zheng, V. N. Strocov, D. S. Sanchez, G. Chang, C. Zhang, D. Mou, Y. Wu, L. Huang, C.-C. Lee, S.-M. Huang, B. Wang, A. Bansil, H.-T. Jeng, T. Neupert *et al.*, Discovery of a Weyl fermion state with Fermi arcs in niobium arsenide, Nat. Phys. **11**, 748 (2015).

[12] M. Z. Hasan and C. L. Kane, Colloquium: Topological insulators, Rev. Mod. Phys. **82**, 3045 (2010).

[13] P. Corbae, S. Ciocys, D. Varjas, E. Kennedy, S. Zeltmann, M. Molina-Ruiz, S. M. Griffin, C. Jozwiak, Z. Chen, L.-W. Wang, A. M. Minor, M. Scott, A. G. Grushin, A. Lanzara, and F. Hellman, Observation of spin-momentum locked surface states in amorphous Bi_2Se_3, Nat. Mater. **22**, 200 (2023).

[14] R. Queiroz, G. Landolt, S. Muff, B. Slomski, T. Schmitt, V. N. Strocov, J. Mi, B. B. Iversen, P. Hofmann, J. Osterwalder, A. P. Schnyder, and J. H. Dil, Sputtering-induced reemergence of the topological surface state in Bi_2Se_3, Phys. Rev. B **93**, 165409 (2016).

[15] J. N. Nelson, A. D. Rice, R. Kurleto, A. Shackelford, Z. Sierzega, P. Hao, B. S. Berggren, C.-S. Jiang, A. G. Norman, M. E. Holtz, J. S. Mangum, I. A. Leahy, K. N. Heinselman, H. Ness, M. Van Schilfgaarde, D. S. Dessau, and K. Alberi, Thin-film TaAs: Developing a platform for Weyl semimetal devices, Matter **6**, 2886 (2023).

[16] M. DC, R. Grassi, J.-Y. Chen, M. Jamali, D. Reifsnyder Hickey, D. Zhang, Z. Zhao, H. Li, P. Quarterman, Y. Lv, M. Li, A. Manchon, K. A. Mkhoyan, T. Low, and J.-P. Wang, Room-temperature high spin–orbit torque due to quantum confinement in sputtered $Bi_xSe_{(1-x)}$ films, Nat. Mater. **17**, 800 (2018).

[17] W. Yanez, Y. Ou, R. Xiao, J. Koo, J. T. Held, S. Ghosh, J. Rable, T. Pillsbury, E. G. Delgado, K. Yang, J. Chamorro, A. J. Grutter, P. Quarterman, A. Richardella, A. Sengupta, T. McQueen, J. A. Borchers, K. A. Mkhoyan, B. Yan, and N. Samarth, Spin and charge interconversion in Dirac-semimetal thin films, Phys. Rev. Appl. **16**, 054031 (2021).

[18] D. Zhang, W. Jiang, H. Yun, O. J. Benally, T. Peterson, Z. Cresswell, Y. Fan, Y. Lv, G. Yu, J. G. Barriocanal, P. W. Swatek, K. A. Mkhoyan, T. Low, and J.-P. Wang, Robust negative longitudinal magnetoresistance and spin–orbit torque in sputtered Pt_3Sn and $Pt_3Sn_xFe_{1-x}$ topological semimetal, Nat. Commun. **14**, 4151 (2023).

[19] C. Lin, M. Ochi, R. Noguchi, K. Kuroda, M. Sakoda, A. Nomura, M. Tsubota, P. Zhang, C. Bareille, K. Kurokawa, Y. Arai, K. Kawaguchi, H. Tanaka, K. Yaji, A. Harasawa, M. Hashimoto, D. Lu, S. Shin, R. Arita, S. Tanda *et al.*, Visualization of the strain-induced topological phase transition in a quasi-one-dimensional superconductor $TaSe_3$, Nat. Mater. **20**, 1093 (2021).

[20] A. Mitra, R. Xiao, W. Yanez, Y. Ou, J. Chamorro, T. McQueen, A. J. Grutter, J. A. Borchers, M. R. Fitzsimmons, T. R. Charlton, and N. Samarth, Constraints on proximity-induced ferromagnetism in a Dirac semimetal (Cd_3As_2)/ferromagnetic semiconductor $(Ga_{1-x}Mn_xSb)$ heterostructure, Phys. Rev. Mater. **7**, 094201 (2023).

[21] J. Mutch, W.-C. Chen, P. Went, T. Qian, I. Z. Wilson, A. Andreev, C.-C. Chen, and J.-H. Chu, Evidence for a strain-tuned topological phase transition in $ZrTe_5$, Sci. Adv. **5**, eaav9771 (2019).

[22] L. Wu, S. Patankar, T. Morimoto, N. L. Nair, E. Thewalt, A. Little, J. G. Analytis, J. E. Moore, and J. Orenstein, Giant anisotropic nonlinear optical response in transition metal monopnictide Weyl semimetals, Nat. Phys. **13**, 350 (2017).

[23] R. Zu, M. Gu, L. Min, C. Hu, N. Ni, Z. Mao, J. M. Rondinelli, and V. Gopalan, Comprehensive anisotropic linear optical properties of the Weyl semimetals TaAs and NbAs, Phys. Rev. B **103**, 165137 (2021).

[24] J. Sadowski, J. Z. Domagała, W. Zajkowska, S. Kret, B. Seredyński, M. Gryglas-Borysiewicz, Z. Ogorzałek, R. Bożek, and W. Pacuski, Structural properties of TaAs Weyl semimetal thin films grown by molecular beam epitaxy on GaAs (001) substrates, Cryst. Growth Des. **22**, 6039 (2022).

[25] A. Bedoya-Pinto, A. K. Pandeya, D. Liu, H. Deniz, K. Chang, H. Tan, H. Han, J. Jena, I. Kostanovskiy, and S. S. P. Parkin, Realization of epitaxial NbP and TaP Weyl semimetal thin films, ACS Nano **14**, 4405 (2020).

[26] S. Li, Z. Lin, W. Hu, D. Yan, F. Chen, X. Bai, B. Zhu, J. Yuan, Y. Shi, K. Jin, H. Weng, and H. Guo, Exploration of growth conditions of TaAs Weyl semimetal thin film using pulsed laser deposition, Chin. Phys. B **32**, 047103 (2023).

[27] I. Vurgaftman, J. R. Meyer, and L. R. Ram-Mohan, Band parameters for III-V compound semiconductors and their alloys, J. Appl. Phys. **89**, 5815 (2001).

[28] See Supplemental Material at http://link.aps.org/supplemental/10.1103/PhysRevMaterials.8.034204 for extended characterization and charge to spin conversion data.

[29] S. Hikami, A. I. Larkin, and Y. Nagaoka, Spin-orbit interaction and magnetoresistance in the two dimensional random system, Prog. Theor. Phys. **63**, 707 (1980).

[30] R. Xiao, S. Islam, W. Yanez, Y. Ou, H. Liu, X. Xie, J. Chamorro, T. M. McQueen, and N. Samarth, Influence of magnetic and electric fields on universal conductance fluctuations in thin films of the Dirac semimetal Cd_3As_2, Nano Lett. **23**, 5634 (2023).

[31] O. Mosendz, V. Vlaminck, J. E. Pearson, F. Y. Fradin, G. E. W. Bauer, S. D. Bader, and A. Hoffmann, Detection and quantification of inverse spin Hall effect from spin pumping in permalloy/normal metal bilayers, Phys. Rev. B **82**, 214403 (2010).

[32] H. Wang, J. Kally, J. S. Lee, T. Liu, H. Chang, D. R. Hickey, K. A. Mkhoyan, M. Wu, A. Richardella, and N. Samarth, Surface-state-dominated spin-charge current conversion in topological-insulator–ferromagnetic-insulator heterostructures, Phys. Rev. Lett. **117**, 076601 (2016).